LA-UR -78-934

TITLE: QUANTUM MECHANICS OF ELECTRONIC-ROTATIONAL ENERGY TRANSFER IN $F(^2P) + H_2$ COLLISIONS

AUTHOR(S): Robert E. Wyatt and Robert B. Walker

SUBMITTED TO: Proceedings of the workshop on Reactive Scattering, Orsay France May - July, 1977

NOTICE

This report was prepared as an account of work sponsored by the United States Government. Neither the United States nor the United States Department of Energy, nor any of their employees, nor any of their contractors, subcontractors, or their employees, makes any warranty, express or implied, or assumes any legal liability or responsibility for the accuracy, completeness or usefulness of any information, apparatus, product or process disclosed, or represents that its use would not infringe privately owned rights.

By acceptance of this article for publication, the publisher recognizes the Government's (license) rights in any copyright and the Government and its authorized representatives have unrestricted right to reproduce in whole or in part said article under any copyright secured by the publisher.

The Los Alamos Scientific Laboratory requests that the publisher identify this article as work performed under the auspices of the USERDA.

los alamos
scientific laboratory
of the University of California
LOS ALAMOS, NEW MEXICO 87545

An Affirmative Action/Equal Opportunity Employer

MASTER

Form No. 836
St. No. 2629
1/75

UNITED STATES
ENERGY RESEARCH AND
DEVELOPMENT ADMINISTRATION
CONTRACT W-7405-ENG. 36

DISTRIBUTION OF THIS DOCUMENT IS UNLIMITED

Quantum Mechanics of Electronic-Rotational Energy Transfer in $F(^2P) + H_2$ Collisions

by

Robert E. Wyatt*
Department of Chemistry
The University of Texas at Austin
Austin, Texas 78712

and

Robert B. Walker†
Theoretical Division
Los Alamos Scientific Laboratory
Los Alamos, New Mexico 87545

*Supported in part by grants from the Robert A. Welch Foundation and the National Science Foundation.

†Work prrformed in part under the auspices of the U. S. Department of Energy.

Abstract

Theoretical study is made of electronic-rotational energy transfer in $F(^2P) + H_2$ three-dimensional collisions, with electronic matrix elements from DIM theory. The quantum close-coupled equations are integrated via the R-matrix propagation method. Inelastic quenching probabilities are emphasized, with and without simulated open reaction channels. Interweaving patterns in the transition probability for even and odd nuclear parity vs. J (total angular momentum quantum number) are analyzed in terms of avoided crossing structure in the electrotational energy correlation diagrams. Localized regions where electronic quenching is dominant are identified in the correlation diagrams, and are confirmed in separate calculations which neglect interchannel mixing in local regions of the atom-molecule separation. Open reaction channels are found to have little influence on the quenching probabilities in these low energy calculations.

I. Introduction

The theoretical study of electronic-nuclear energy transfer in molecular collisions has recently intensified.[1,2] Quantum collinear studies of $X(^2P) + H_2$ (X = halogen) nonreactive collisions,[3] $Ba + N_2O$ or $H^+ + H_2$ collinear reactive collisions,[4,5] and three-dimensional $C^+(^2P) + H_2$ nonreactive collisions[6] (following a formulation emphasizing $H^+ + F$ atomic collisions[7]) have recently appeared. In addition, coplanar[8] and three-dimensional[9,10] studies of nonreactive $F(^2P) + H_2$ collisions which employ the quantum close-coupling method have emphasized the realtive ease of electronic-rotational energy transfer in the near-resonant quenching process: $F(^2P_{\frac{1}{2}}) + H_2(j=0) \rightarrow$ $\rightarrow F(^2P_{3/2}) + H_2(j=2)$. Semiclassical studies of $F(^2P_{\frac{1}{2}}) + H_2$ $\rightarrow FH + H$ reactive collisions[11,12] have suggested the importance of this channel at higher collision energies.

In this study, probabilities and cross sections for electronic-rotational energy tannsfer in inelastic $F(^2P_{\frac{1}{2}})$ $+ H_2(j=0)$ collisions are calculated through integration of the quantum mechanical close-coupling equations. Competition between the near-resonant and nonresonant processes (leading to $F(^2P_{3/2}) + H_2(j=2)$ or $F(^2P_{3/2}) + H_2(j=0)$, respectively) is studied as a function of both J (total angular momentum quantum number) and E_{tr} (reactant translational energy). All electronic information concerning the ground and excited states is obtained from Diatomics-in-Molecules (DIM) theory.[13-15] Utilization of DIM electronic-nuclear basis functions, which serve as an expansion basis for the scattering wavefunction, has been discussed previously.[16,17]

In Sec. IIA, the generation of electrotational basis functions through angular momentum coupling of products of DIM electronic functions and nuclear tumbling-bending functions is reviewed. The matrix representation of the Hamiltonian in this basis is discussed. (The total Hamiltonian is partitioned into a sum of translation, electronic, and rotational components $\hat{H} = \hat{T}_s + \hat{H}_{el} + \hat{T}_{rot}$, where the electronic Hamiltonian is further decomposed into the sum of spin-free and atomic spin-orbit interaction terms, $\hat{H}_{el} = \hat{H}^{SF}_{el} + \hat{H}_{so}$. In the electrotational basis, $\hat{H}_{so}$ is diagonal.) Natural collision coordinates[18,19] are defined to specify the orientation, size, and shape of the nuclear triangle. Then, in Sec. IIB, use of the recently developed R-matrix propagation method[20a] for numerical integration of close-coupled equations for the translational scattering wavefunctions is reviewed. Boundary conditions on the scattering wavefunction are discussed in Sec. IIC. Boundary conditions, in terms of the S-matrix, are described for both "pure" inelastic collisions and for inelastic collisions in the presence of open reaction channels which are simulated by detailed quantum transition state theory[21] (DQTST).

The energy and angular momentum dependence of the near-resonant and nonresonant quenching probabilities is illustrated in Sec. IIIA, while the energy dependence of the yields and cross sections are shown in Sec. IIIB. Then, in Sec. IIIC, interesting alterations in the resonant transition probability

accompanying variations in J are related to avoided crossing structure in electrotational adiabatic energy correlation diagrams. In Sec. IIID, quantitative examination is made of the localized region (of atom-molecule separations) which dominates the electronic quenching process. Finally, the first quantum results on the influence of reaction channels on the low energy nonreactive quenching process are examined in Sec. IIID. Further discussion and conclusions are presented in Sec. IV.

II. Theory

A. Electrotational Basis

1. Coordinates

Natural collision coordinates will be used to specify the size and shape of the instantaneous three-body triangle.[18,19] The triangle orientation relative to nonrotating axes is specified by three Euler angles θ, ϕ, χ. Fig. 1 shows the collinear $F + H_2$ coordinate plane, where Z and z are the components of $\vec{R}$ and $\vec{r}$ on the (body-fixed) rotating z-axis. $\vec{R}$ and $\vec{r}$ are scaled atom-molecule and molecular vectors, respectively: $\vec{R} = \vec{R}$ (unscaled)/(0.725) and $\vec{r} = \vec{r}$ (unscaled)(0.725). The scale factor is chosen so that within the scaled coordinate system, the nuclear reduced mass is the same for translation, vibration and rotation: $2\mu/\hbar^2 = 128.405 a_0^{-2} eV^{-1}$. The collinear space is divided into polar and Cartesian regions in Fig. 1. The natural coordinate s is the arc length measured along the reference curve (RC), with s = 0 on the reactant-product match surface M, and $s \to -\infty$ as the $F + H_2$ distance increases. The two other natural coordinates, ρ and γ are the polar coordinates of a point in a constant s plane. The three natural coordinates s, ρ, and γ thus define nuclear translational, vibrational, and bending motions within the rotating coordinate system. The electronic coordinates are also assumed to be specified within the rotating coordinate system.

The orientation of the body-fixed z-axis relative to the nuclear triangle is determined by a switching angle $\alpha(s)$. In these calculations, α is chosen so that the body-fixed z-axis

coincides with the $\vec{R}$ direction in the Cartesian region ($s < s$) of Fig. 1. The switching angle explicitly enters the rotational kinetic energy later in Eq. 8 through the function f(s), where $f = \cos(\alpha-\psi)$, with angle ψ defined in Fig. 1.

Since our emphasis is on low energy electronic-rotational energy transfer, vibrational nonadiabatic effects are not considered. The vibrational coordinate ρ in Fig. 1 was adjusted (at each s) to lie on the reaction path (RP) on the ground electronic state adiabatic potential surface.

2. Electronic Matrix Elements

All input from the electronic problem is provided by DIM theory. Following Miller and Wyatt,[17] a matrix representation of $\hat{H}^{SF}_{el}$ is constructed in the electronic spin-coupling scheme $(S_F\ S_A)S_{FA}(S_{FA}S_B)S$, where S_j is the atomic spin on atom j. A minimal basis containing six ^2P F-atom states, and two ^2S states on each hydrogen atom are used to construct 24 atomic product functions, in terms of which the 24 spin coupled polyatomic basis functions are constructed. The axis of quantization for electronic angular momentum is along the body-fixed z-axis. The nondiagonal matrix $\underline{\underline{H}}^{SF}_{el}$ (24 x 24) has matrix elements composed of linear combinations of the $^1\Sigma$ and $^3\Sigma$ H_2 diatomic potentials, and the $^1\Sigma$, $^3\Sigma$, $^1\pi$, and $^3\pi$ HF diatomic potentials. All parameters in these potential curves are tabulated by Tully[13] (Table V, Calculation II).

Before injecting this electronic information into the electrotational basis functions, the electronic angular momentum

is recoupled according to the scheme: $(L_F S_F)J_F(S_A S_B)S_H(J_F S_H)J_e$. The total electronic angular momentum component K_e is again defined along the z-axis. Counting K_e values, there are 24 values of the electronic index σ, which combines the coupling scheme index with the appropriate K_e value (see Table I in Ref. 17). For each value of s, ρ, and γ, the electronic matrix elements are denoted $H_{\sigma'\sigma}(s,\rho,\gamma)$. In this representation, the atomic spin-orbit interaction $\lambda\vec{L}_F\cdot\vec{S}_F$ is diagonal. The appropriate spin-orbit energy is added to each diagonal element after converting the matrix representing $\hat{H}^{SF}_{el}$ into the new coupling scheme: $\underline{\underline{H}}_{el}(s,\rho,\gamma) = \underline{\underline{T}}\,\underline{\underline{H}}^{SF}_{el}(s,\rho,\gamma)\underline{\underline{T}}^{+} + \underline{\underline{H}}_{so}$ where $\underline{\underline{T}}$ is a complex 24 x 24 matrix.

As functions of γ, the electronic matrix elements show tensor character in that the angular dependence is like an associated Legendre polynomial:

$$H_{\sigma'\sigma}(s,\rho,\gamma) \sim P_{\lambda}^{|K_e-K_e'|}(\cos\gamma). \tag{1}$$

Even <u>or</u> odd reflection symmetry about $\gamma = \pi/2$ is determined by whether $S_H' - S_H + K_e' - K_e$ is even or odd, respectively. In calculating angular averages, the following expansion is useful (only even <u>or</u> odd symmetry Legendre polynomials are included):

$$H_{\sigma'\sigma}(s,\rho,\gamma) = \sum_{\lambda=\lambda_{min},\lambda_{min}+2,\ldots} C^{\lambda}_{\sigma'\sigma}(s,\rho)\,P_{\lambda}^{|K_e-K_e'|}(\cos\gamma), \tag{2}$$

where the minimum value of the expansion index is

$$\lambda_{min} = \begin{cases} |K_e' - K_e| & , S_H' - S_H + K_e' - K_e = \text{even}, \\ |K_e' - K_e| + 1 & , S_H' - S_H + K_e' - K_e = \text{odd}. \end{cases} \tag{3}$$

In practice, a three term expansion of each electronic matrix element is used. The expansion coefficients are found by requiring that the sum on the right side of Eq. 2 exactly reproduce the value of $H_{\sigma'\sigma}$ at three angles. (For $\Delta K_e = 0$, the angles $\gamma = 0$, $\pi/4$, and $\pi/2$ were used, and for $\Delta K_e \neq 0$, the angles $\gamma = \pi/8$, $\pi/4$, and $3\pi/8$ were used).

3. Electronuclear Basis

A convenient basis for expansion of the scattering wavefunction are the combined electronic-rotational functions defined by Miller and Wyatt.[17] These functions are sums of products of DIM electronic functions $\{\phi_\sigma^{DIM};\ \sigma = 1,2\cdots 24$ and nuclear rotational functions $\{N_{MK}^J(\theta\phi\chi)\phi_{j\ell}^{L_nK_n}(\gamma)\}$, where N_{MK}^J is a normalized symmetric top function, and $\phi_{j\ell}^{L_nK_n}$ is a free internal rotor function.[17,23] The electronic and rotational angular momenta are coupled according to the scheme labeled by indices α,

$$\alpha = \underbrace{(L_FS_F)J_F(S_AS_B)S_H(J_FS_H)J_e}_{\text{electronic}}\underbrace{(\ell j)L_n}_{\text{nuclear}}\underbrace{(L_nJ_e)J}_{\text{total}} \tag{4}$$

The electrotational functions are then

$$\Omega_\alpha^{JM}(\theta\phi\chi\gamma e) = \left(\frac{2L_n+1}{2J+1}\right)^{1/2} \sum_{K_eK_n} N_{MK}^J(\theta\phi\chi)\phi_{j\ell}^{L_nK_n}(\gamma)\phi_\sigma^{DIM}(e)\langle L_n\bar{L}_eK_nK_e|JK\rangle \tag{5}$$

where $\langle J_1 J_2 K_1 K_2 | JK \rangle$ is a Clebsch-Gordan coefficient. These functions are orthonormal when integrated over all electronic and rotational coordinates, $\langle \Omega_\alpha^{JM} | \Omega_{\alpha'}^{JM} \rangle = \delta_{\alpha\alpha'}$.

4. Representation of $\hat{H}_{el}$ in Electrotational Basis

In the close coupling method, electronic-rotational channels (labeled by the index α) are coupled through matrix elements $\langle \Omega_{\alpha'}^{JM} | \hat{H}_{el} | \Omega_\alpha^{JM} \rangle$. When Eq. 5 for Ω_α^{JM} or $\Omega_{\alpha'}^{JM}$ is used, the required matrix elements involve sums of angular integrals of the electronic matrix elements, $\langle \phi_{\sigma'}^{DIM} | \hat{H}_{el} | \phi_\sigma^{DIM} \rangle = H_{\sigma'\sigma}$. When Eq. 2 is used for the angular dependence of the electronic matrix elements, we obtain the matrix elements (integration over θ, ϕ, χ, γ, and e has been completed

$$\langle \Omega_\alpha^{JM} | \hat{H}_{el} | \Omega_{\alpha'}^{JM} \rangle = \sum_{K_e K_e' \lambda} C_{\sigma\sigma'}^{\lambda}(R,\rho)\, F_{\alpha K_e \alpha' K_e'}^{J\lambda} , \tag{6}$$

where the F-coefficients are completely independent of geometry. They are sums of products of Clebsch-Gordan coefficients,

$$\begin{aligned} F_{\alpha K_e \alpha' K_e'}^{J\lambda} = & \left[\frac{(2\ell+1)(2\ell'+1)}{(2J+1)^2}\right]^{1/2} \sum_{K_n} \langle L_n J_e K_n K_e | JK \rangle \langle L_n' J_e', K-K_e' | JK \rangle \\ & \times \langle \ell j 0 K_n | L_n K_n \rangle \langle \ell' j' 0, K-K_e | L_n', K-K_e' \rangle S_{K_n} S_{K_n'} \\ & \times \langle P_{j'}^{|K_n'|} | P_n^{|K_e-K_e'|} | P_j^{|K_n|} \rangle_\gamma , \end{aligned} \tag{7}$$

where the phase factor S_{K_n} arises in the definition of the spherical harmonics,[24] $S_{K_n} = (-1)^{K_n}$, $K_n < 0$ and $S_{K_n} = +1$, $K_n > 0$. The integral over the product of three Legendre polynomials

may be evaluated in terms of Clebsch-Gordan coefficients.[24] In our computations, the F-coefficients are computed (and stored on the disk) at the first step of integration of the close-coupled scattering equations. The same set of F's are used at each step of the integration process.

5. Representation of $\hat{H}_{rot}$ in Electrotational Basis

The representation of the rotational kinetic energy operator $\hat{T}_{rot}$ (which includes contributions from overall triangle tumbling, and from internal bending) in the electrotational basis has been derived by Miller and Wyatt.[17] To a good approximation the rotational kinetic energy operator is diagonal in this basis, with eigenvalues given by

$$W_{j\ell}^{L_n}(s) = AL_n(L_n+1) + Bj(j+1) + f\,A\left[L_n(L_n+1) + j(j+1) - \ell(\ell+1)\right], \quad (8)$$

where (see Fig. 1 for definitions of R_p and r_p):

$$A = \frac{\hbar^2}{2\mu(R_p^2 - r_p^2 f^2)}, \quad B = A\left(\frac{R_p}{r_p}\right)^2, \quad f = \frac{2}{\pi}\tan^{-1}(9s). \quad (9)$$

The function f(s) controls the orientation of the rotating z-axis with respect to the nuclear framework. As $s \to -\infty$, $f \to -1$ and the rotational eigenvalues correctly become

$$W_{j\ell}^{L_n} = \frac{j(j+1)\hbar^2}{2\mu z^2} + \frac{\ell(\ell+1)\hbar^2}{2\mu Z^2}, \quad (10)$$

where z is the scaled H_2 intermolecular separation, and $Z = (R_p^2 - r_p^2)^{\frac{1}{2}}$ is the scaled atom-molecule separation. For this choice for f, the asymptotic form for the rotational energy is reached just after the Cartesian region of Fig. 1 is entered (starting from s = 0). The rotational eigenvalues at the s = 0 limit become (with f = 0 and $R_p = r_p$)

$$W_{j\ell}^{L_n}(0) = \frac{\hbar^2}{2\mu R_p^2}\left[L_n(L_n+1) + j(j+1)\right] \tag{11}$$

6. Expansion of Scattering Wavefunction

The scattering wavefunction at total angular momentum J and input channel α (defined earlier in Eq. 4) may be expanded in the electrotational basis,

$$\Psi_\alpha^J(\theta\phi\chi\gamma e\Delta) = \mathcal{J}\sum_{\alpha'=1}^{N} T_{\alpha'\alpha}^J(\Delta)\,\Omega_\alpha^{JM}(\theta\phi\chi\gamma e), \tag{12}$$

where the $\{T_{\alpha'\alpha}^J\}$ are translational wavefunctions. In addition, $\mathcal{J}$ is a scale factor which is chosen to simplify the form of the close-coupled equations for the translational wavefunctions. We define $\mathcal{J}$ to be $(R_p^2 - f^2 r_p^2)^{-\frac{1}{2}}$, which becomes R^{-1} at large atom-molecule separations. The expansion in Eq. 12 does not include vibrational states, because our emphasis is on electronic-rotational energy transfer in low energy atom-diatom collisions. The theory could easily be extended to include vibrational effects, at the expense of greater computer time. The close-coupled equations for the translational wavefunctions are derived by requiring

$$\langle \Omega^{JM}_{\alpha'} | \hat{H} - E | \Psi^{JM}_{\alpha} \rangle = 0, \quad \alpha' = 1, 2 \cdots N, \tag{13}$$

The electrotational channels are coupled through the interaction matrix, which has elements $B^J_{\alpha\alpha'} = \langle \Omega^{JM}_{\alpha} | \hat{H}_{el} + \hat{T}_{rot} | \Omega^{JM}_{\alpha'} \rangle$. The close-coupled equations are then

$$\left(\frac{d^2}{dR^2} - \frac{2\mu E}{\hbar^2} \right) T^J_{\alpha'\alpha}(R) = \sum_{\alpha''=1}^{N} B^J_{\alpha'\alpha''}(R) T^J_{\alpha''\alpha}(R). \tag{14}$$

B. Solution of the Close-Coupled Equations

The close coupled equations for translational motion are solved by the R-matrix propagation technique described by Light and Walker.[20a] The R-matrix defines the relationship between the translational functions and their derivatives at both ends of the integration range, so that

$$\begin{bmatrix} \underline{\underline{I}}^J(Q_0) \\ \underline{\underline{I}}^J(Q_f) \end{bmatrix} = \begin{bmatrix} \underline{\underline{R}}_1 & \underline{\underline{R}}_2 \\ \underline{\underline{R}}_3 & \underline{\underline{R}}_4 \end{bmatrix} \begin{bmatrix} \frac{d}{dQ}\underline{\underline{I}}^J(Q_0) \\ -\frac{d}{dQ}\underline{\underline{I}}^J(Q_f) \end{bmatrix} \tag{15}$$

where s is the scattering coordinate and s_o and s_f specify its initial and final values. The R-matrix is determined by dividing configuration space into sectors each spanning a small range of the scattering coordinate. The size of each sector is chosen small enough that the coupling matrix in Eq. 14 may be accurately regarded as constant over the entire sector width. The coupling matrix is then diagonalized and the wavefunction expansion is transformed to the locally uncoupled representation. In this representation, a local sector R-matrix (satisfying boundary relationships as in Eq. 15, but spanning only the local sector) is determined analytically. The sector R-matrices and the appropriate sector to sector basis transformation matrices are assembled recursively using the formulas originally derived by Zvijac and Light.[20b]

The R-matrix propagation method has two distinct advantages for this problem. The linear independence of translational solutions to the coupled equations are unaffected by the presence

of any number of closed channels, no matter how deeply buried. All channels which correlate to excited electronic species of $F + H_2(^3\Sigma)$ are very deeply buried; in this method, these channels cause no difficulty whatsoever. The R-matrix propagation method is also desirable for this problem because the evaluation of the coupling potential is very time-consuming. Because the step size algorithm for the R-matrix propagation method is the same as that used in the Magnus propagation method,[20c] a smaller number of potential evaluations are required as compared to methods which integrate the translational functions and their derivatives directly. Furthermore, because the step size algorithm is independent of the scattering energy, the potential evaluation is performed only once in each sector for the initial scattering energy. Consequently, we obtain a very significant improvement in the time required to perform a scattering calculation after the first energy. For example, most calculations performed here required approximately six minutes of CDC6600 time for the first scattering energy at each J, and only ten seconds per energy thereafter.

The R-matrix propagation scheme operates differently in the two different $F + H_2$ scattering problems considered here. In the first model, we consider only inelastic scattering events, and the scattering wavefunction is forced to obey regular boundary conditions near the origin ($s=0$). For this reason, only the subset of R-matrix propagation equations necessary to asymptotically determine the R_4 block (an N x N matrix, for N

channels) of the R-matrix are involved. Consequently, the inelastic scattering calculation requires only half the effort necessary to determine the full R-matrix. In the second model, the detailed quantum transition state theory (DQTST) of Light and Siczek[21] is employed to investigate the relative importance of reactive scattering vents from the two possible initial spin orbit levels of fluorine. In this case, a transition state theory assumption is made on the inner R-matrix boundary (near s=0), that all flux locally penetrating this surface continues on towards the asymptotic product region of configuration space with no back reflection. In this case, regular boundary conditions are not assumed on the transition state surface (TSS) and the full R-matrix (a 2N x 2N matrix) must be computed. The boundary conditions employed in the two scattering models treated here are discussed in more detail in the following section.

C. Boundary Conditions

Boundary conditions for the F + H_2 inelastic scattering problem are applied in the normal fashion. At large atom-molecule separations, the scattering wavefunction assumes the asymptotic form

$$\Psi_\alpha^{JM}(\theta\phi\chi\gamma e s) = (k_\alpha R)^{-1} \exp[-i(kR - \ell\pi/2)]\,\Omega_\alpha^{JM}(\theta\phi\chi\gamma e) - \sum_{\alpha'=1}^{N} (k_{\alpha'} R)^{-1} \exp[+i(k_{\alpha'} R - \ell'\pi/2)]\,\Omega_{\alpha'}^{JM}(\theta\phi\chi\gamma e)\left(\frac{k_{\alpha'}}{k_\alpha}\right)^{1/2} S_{\alpha'\alpha}^{J} \cdot \quad (16)$$

An equation similar to Eq. 16 also holds for the derivative of the wavefunction. Both equations are cast in matrix form and are combined with the equation for the R_4 block of the R-matrix, $\underline{\underline{T}}^J(s_f) = (\underline{\underline{R}}_4)\cdot(\underline{\underline{T}}^{J'}(s_f))$, to give a matrix equation for the scattering matrix S in terms of the R-matrix. We obtain

$$\underline{\underline{S}} = \underline{\underline{k}}_\infty^{+1/2}\, \underline{\underline{W}}^{-1}\, \underline{\underline{W}}^{*}\, \underline{\underline{k}}_\infty^{-1/2} \quad (17)$$

$$\underline{\underline{W}} = \underline{\underline{R}}_4 \underline{\underline{O}}'_\infty - \underline{\underline{O}}_\infty \quad (18)$$

where $\underline{\underline{k}}_\infty$ is a diagonal matrix of the asymptotic channel momenta and $\underline{\underline{O}}_\infty$ ($\underline{\underline{O}}'_\infty$) is the diagonal matrix of asymptotic channel translational functions (and their derivatives), so that

$$(O_\infty)_{\alpha\alpha'} = \delta_{\alpha'\alpha}\, i k_\alpha^{-1} h_\ell^{(1)}(k_\alpha R),$$
$$(O_\infty)_{\alpha\alpha'} = \delta_{\alpha'\alpha}\, i\, h_\ell^{(1)\prime}(k_\alpha R), \tag{19}$$

where $h_\ell^{(1)}$ is a spherical Ricatti-Hankel function. For closed channels, the appropriate Hankel functions of imaginary argument are used. All features of the collision process are then determined from the S-matrix.

When the DQTST model is applied to the scattering process in order to estimate the relative importance of reactive scattering from each initial spin orbit state of fluorine, the boundary conditions applied to the R-matrix are slightly different. Asymptotically, at large F to H_2 distances, the wavefunction assumes the same form as in Eq. 16. However, on the TSS, boundary conditions appropriate to DQTST are applied. The transition state surface is placed near s = 0, and all flux passing through this surface is assumed to be outgoing towards the H + HF products. The scattering wavefunction beyond the TSS assumes the form

$$\Psi_\alpha^{JM}(\theta\phi\chi\gamma e s) = -\sum_{\alpha'=1}^{N} (\tilde{k}_{\alpha'} R)^{-1} \exp[i(kD - \ell'\pi/2)] \times \tilde{\Omega}_{\alpha'}^{JM}(\theta\phi\chi\gamma e) \left(\frac{\tilde{k}_{\alpha'}}{k_\alpha}\right)^{1/2} S_{\alpha'\alpha}^{J(+)} \tag{20}$$

where the internal states $\tilde{\Omega}^{JM}_{\alpha'}$ are the locally adiabatic states on the TSS and the channel momenta $\tilde{k}_{\alpha'}$ are those appropriate to the local channel energies on the TSS. This choice of boundary conditions corresponds to the case (B) discussed by Light and Siczek.[21] The DQTST boundary conditions lead to an equation for the (new) S-matrix similar to that of Eq. (17) and Eq. (18), except that now we have

$$\underline{\underline{k}} = \begin{bmatrix} \underline{\underline{\tilde{k}}} & \underline{\underline{0}} \\ \underline{\underline{0}} & \underline{\underline{k}}_\infty \end{bmatrix}, \tag{21}$$

$$\underline{\underline{W}} = \begin{bmatrix} \underline{\underline{R}}_1 \underline{\underline{\tilde{O}}}' - \underline{\underline{\tilde{O}}} & \underline{\underline{R}}_2 \underline{\underline{O}}'_\infty \\ \underline{\underline{R}}_3 \underline{\underline{\tilde{O}}}' & \underline{\underline{R}}_4 \underline{\underline{O}}'_\infty - \underline{\underline{O}}_\infty \end{bmatrix}. \tag{22}$$

As appropriate for DQTST, no particular relevance is attributed to <u>individual values</u> of the "reactive" S-matrix elements determined by this method. The DQTST approximation seeks only to determine the <u>total</u> flux through the transition state surface in terms of the total reaction probability from a specific initial state of reactants. This total reaction probability is

$$P^J_{\alpha,\,\text{reactive}} = \sum_{\alpha'=1}^{N^{TSS}_{open}} \left| S^{J(+)}_{\alpha'\alpha} \right|^2 \tag{23}$$

where the sum runs over all states locally open on the TSS.

III. Close-Coupling Results

A. Transition Probabilities

Through use of the R-matrix propogation technique, we have integrated systems of close-coupled equations to obtain transition probabilities as functions of E and J for the near-resonant and nonresonant quenching of electronically excited F in collisions with H_2:

$$F(^2P_{3/2}) + H_2(j=0) \rightarrow \begin{cases} F(^2P_{\frac{1}{2}}) + H_2(j=2) & \text{near-resonant} \\ F(^2P_{\frac{1}{2}}) + H_2(j=0) & \text{non-resonant} \end{cases}$$

Results will first be considered for purely nonreactive processes on a DIM electronic basis which excludes $^3\Sigma$ H_2 contributions. The resultant surfaces at small R are repulsive; the lowest adiabatic surface does not decline into an exoergic FH + H exit valley. Later, in Section IIIE, DQTST results will be described for the quenching process in the presence of simulated reaction channels.

The results in this section were obtained with electrotational bases containing j=0 and 2 H_2 rotational states, $J_F = \frac{3}{2}$ and $\frac{1}{2}$ electronic states, and all nuclear rotational states labeled by ℓ and L_n which are consistent with having a specified value of J. For $J = \frac{1}{2}$, this involves 8 channels for even or odd nuclear parity, which is determined by the values of ℓ and L_n. The number of states gradually increases with increasing J, and includes 18 states when $J \geq 7/2$.

In Fig. 2, resonant transition probabilities vs. J are shown for two different translational energies, 0.012 eV and 0.035 eV. The upper energy is just below the threshold (0.045 eV translational energy) for the $F(^2P_{\frac{1}{2}}) + H_2(j=2)$ channel. These transition probabilities are sums over probabilities into all final ℓ' and L_n' channels consistent with the specified total value of J:

$$P_{res}^{J(\pm)} = \sum_{L_n'=|J-J_F'|}^{J+J_F'} \sum_{\ell'=|L_n'-j'|}^{L_n'+j'} \left| S^J_{\alpha'\alpha} \right|^2 , \qquad (1)$$

where $J_F' = \frac{3}{2}$ and $j' = 2$. Transition probabilities are shown for both even and odd nuclear parity. The nuclear parity (±) is determined by whether $j + \ell$ is an even or odd integer, rsspectively. In this case, since j=0, the value of ℓ completely determines the nuclear parity. (For $F + H_2$ <u>non</u>reactive collisions, the four symmetry types determined by even <u>or</u> odd values of j <u>and</u> $j + \ell$ decouple the scattering problem into four noninteracting categories.) Fig. 2a shows a very interesting interweaving of $P_{res}^{J(+)}$ and $P_{res}^{J(-)}$ as they decline from the values at $J = \frac{1}{2}$, followed by an abrupt change near J = 23/2. For J > 33/2, the transition probabilities then rapidly decrease in magnitude. A similar qualitative pattern is shown at higher energy in Fig. 2b, with the alteration in the regular pattern at low J now occurring near J = 31/2. The interweaving of $P_{res}^{J(+)}$ and $P_{res}^{J(-)}$ and the alteration in this pattern at higher

J, are correlated with avoided crossing structure in the electrotational energy correlation diagrams (see Sec. IIIC). A similar pattern with increasing J was obtained by Chu and Dalgarno[6] (see the partial cross sections in their Fig. 2) in close-coupling studies of $C^+(^2P_{\frac{1}{2}}) + H_2(j=0) \rightarrow C^+(^2P_{3/2}) + H_2(j=0)$ collisions at $E_{tr} = 0.0275$eV.

Finally, Fig. 3 shows the dependence upon energy of the resonant and nonresonant transition probabilities for the lowest partial wave, $J = \frac{1}{2}$. The rapid growth of the resonant probability just above threshold should be noted.

B. Cross Sections

For initial and final channels that involve $^1\Sigma$ H_2 ($S_H = S_H' = 0$, so that $J_F = J_e$ and $J_F' = J_e'$), the degeneracy averaged cross section leading from an input channel $J_F j$ to the final channel $J_F' j'$ is (cross section formulas for F + H_2 collisions are discussed by Rebentrost and Lester[10]):

$$\sigma_{J_F j J_F' j'} = \frac{\pi}{(2j+1)(2J_F+1)k^2_{J_F j}} Y_{J_F j J_F' j'} \tag{2}$$

where the yield is

$$Y_{J_F j J_F' j'} = \sum_{J=\frac{1}{2},\frac{3}{2}\ldots} \sum_{L_n=|J-J_F|}^{J+J_F} \sum_{L_n'=|J-J_F'|}^{J+J_F'} \sum_{\ell=|L_n-j|}^{L_n+j} \sum_{\ell'=|L_n'-j'|}^{L_n'+j'} \times (2J+1)\left|S^J_{\alpha'\alpha}\right|^2. \tag{3}$$

In Fig. 4, the yield and cross sections for the resonant and nonresonant quenching processes are shown as functions of translational energy. Except for $E_{tr} \lesssim 0.002$ eV, the resonant process dominates the nonresonant one by a factor of about 10. The sudden increase in σ_{res} for $E_{tr} \lesssim 0.002$ eV is due to the $k_{J_F J}^{-2}$ factor in Eq. 2 multiplying the yield, while the yield is increasing roughly as $k_{J_F J}$. This type of low energy behavior was not reported by Rebentrost and Lester,[10] whose long range potential is probably considerably different from the DIM behavior. The sensitivity of these results to alterations in the long range F - H_2 potential needs to be investigated.

C. Adiabatic Energy Correlation Diagrams

Much of the structure in the dependence of the resonant transition probabilities $P_{res}^{J(+)}$ on J, as shown in Fig. 2, can be at least qualitatively understood by considering the electrotational adiabatic energy correlation diagrams. By diagonalizing the local coupling matrix at the center of each R-matrix sector (See Sec. IIB), we obtain the perturbed stationary state energies $\lambda_\alpha^2(s) = \frac{2\mu}{\hbar^2}\,\varepsilon_\alpha(s)$ as a function of the reaction coordinate s. In Fig. 5a the energy correlation diagram is shown for the J = 0.5 total angular momentum state. The electrotational basis used to construct Fig. 5a includes all channels asymptotically correlating to F + H_2 states with J_F = 1.5, j = 0,2,4 and J_F = 0.5, j = 0,2. The asymptotic splitting between the final states J_F, j = 0.5,0 and 1.5,2 is too small to be seen in the second lowest energy grouping in this figure. Fig. 5a shows clearly the repulsive nature of the F + H_2 interaction at small values of s when no $^3\Sigma$ states of H_2 are included in the electrotational basis. A more detailed view of the energy correlation diagram is presented in Fig. 5b, which shows only the large s behavior of those states directly participating in the resonant quenching process. At the largest F - H_2 separation (s = -6.6 bohrs) the splitting of the (0.5,0) and (1.5,2) states is now evident. It is also seen that two of the four (1.5,2) states experience a repulsive interaction much like the (0.5,0) state, while the other two states experience an attractive long range interaction. It may also be seen that the (0.5,0) diabatic basis state crosses

under the repulsive (1.5,2) states between s = -5 bohrs and s = -6 bohrs. The coupling between these channels near these avoided crossings is responsible for the electronic to rotational energy quenching process.

The interweaving of the resonant transition probabilities as a function of J (seen in Figs. 2a and 2b, and referred to in Sec. IIIA) is consistent with the avoided crossing structure of the higher J energy correlation diagrams. In Figs. 6a-f we show a sequence of correlation diagrams for J = 6.5, 7.5, and 8.5 for both even and odd nuclear parity states. Once again we concentrate on the large s portion of the diagrams near the (0.5,0) and (1.5,2) avoided crossings. For the larger J states, there are ten channels correlating to the (1.5,2) asymptotic level, corresponding to all different possibilities for the values of ℓ and L_n. Five of the ten channels experience a repulsive long range interaction, and the remaining five experience an attractive long range interaction. It may also be seen that the ten channels in the (1.5,2) grouping fall into four separate manifolds, split asymptotically only by the centrifugal potential $\ell(\ell+1)/R^2$. As in Fig. 5, we see the effect of the (0.5,0) diabatic state crossing under the five repulsive channels emanating from the (1.5,2) grouping. Channel coupling at these crossings accounts for the near resonant electronic to rotational energy transfer process. Inspection of Fig. 6 indicates that the interweaved pattern of resonant transition probabilities is always characterized by collisions

in which the initial orbital angular momentum ℓ of the $F(^2P_{\frac{1}{2}}) + H_2(j=0)$ pair is given by $\ell = J - 0.5$. If we then recall that all the positive nuclear parity collisions involve even orbital angular momenta for this transition, it may be seen that the enhanced transition probabilities occur at alternate total angular momentum states for a given nuclear parity.

It is also not surprising that we find relatively large quenching probabilities in those channels which attempt to cross the upper electronic state nearest the classical turning point. When a surface crossing occurs extremely near the classical turning point, we find the enhanced transition probabilities seen at larger J values in Fig. 2a (J = 11.5,12.5) and in Fig. Fig. 2b (J = 16.5 to 21.5). As the value of J increases even further, the series of crossing points (at fixed total energy) moves inside the classically forbidden region, accounting for the rapid dropping off of the transition probability at higher J's.

D. Location of Electronic Transitions.

In order to confirm the region in s where the near-resonant quenching transition is concentrated, we repeated close-coupling calculations for $J = \frac{1}{2}$ (even nuclear parity) with the nonadiabatic coupling neglected in the preselected interval from s_{min} to s_{max}. The same coupling matrix $\underline{\underline{B}}^J$ in Eq. 14 was used to compute local adiabatic eigenvalues and eigenvectors in each s-sector of the R-matrix propagation scheme. But, in these calculations, the sector-to-sector overlap matrix ($\mathcal{S}(i-1,i)$ in Eq. 34 of Ref. 20a) was reset to the unit matrix for all sector transformations in the specified interval. Fig. 7 shows the energy dependence of the resonant transition probability for both the "exact" and modified calculations. When examining the figure, it is helpful to refer back to the $J = \frac{1}{2}$ adiabatic energy correlation diagram in Fig. 5. From Fig. 7, it is apparent that the quenching transition does not arise primarily in the region where $s > -4.6a_o$ (this corresponds to unscaled atom-molecule separations (R(unscaled) $< 6.6\ a_o$). However, when the overlap matrices are unitized over the interval from -4.8 to $-6.4\ a_o$, the resonant transition probability is only 1/5 of the exact value. Examination of Fig. 5 shows that this is the same interval where there are avoided crossings between the $j=0$, $J_F = \frac{1}{2}$ input channel and the upper two channels correlating with $j=2$, $J_F = \frac{3}{2}$. Hence the electronic transition region is fairly localized cround this large R avoided crossing region.

E. Reactive Modeling

Reaction channels were simulated for $J = \frac{1}{2}$ by applying outgoing boundary conditions (in the +s "product" direction) near $s = -0.8\ a_o$. An open channel outgoing wave boundary condition using the local (rather than asymptotic) channel energy was applied to the lowest channel in Fig. 5a, and closed channel boundary conditions were applied to all other channels at this s-value. The results to be described were not sensitive to the actual position where the outgoing boundary conditions were applied. For the $F + H_2$ reaction, the DQTST assumption is not entirely correct, since some flux does reflect back from the near entrance to the product valley. It is likely that the DQTST conditions applied near $s = -0.8\ a_o$ lead to an overestimation of the reaction probability.[22] The resonant and nonresonant quenching probabilities, $P^{J(+)}_{res}$ and $P^{J(+)}_{nonres}$ were found to agree with the previous results (obtained in the "pure" nonreactive model) to better than 1% at all energies shown in Fig. 3 (at the highest energies studied, $P^{J(+)}_{reactive} \approx 0.1 \times P^{J(+)}_{nonres}$). The low energy quenching process is not perturbed by opening the reaction channel. However, this result may certainly change as the system energy increases (the reaction probability from the excited electronic channel increases by a factor of about 200 over the energy range studied). The DQTST simulation was not studied at higher E, or for $J > \frac{1}{2}$.

It is also likely that the total reaction probability from the $J_F = 0.5$, $j = 0$ initial state will increase significantly, when calculations are performed including $^3\Sigma$ states of H_2 in the electrotational basis. As we have seen, this state "crosses" only the subset of states in the lower electronic manifold experiencing a repulsive long range interaction. At the energies studied here, these states are locally closed at the TSS used in the DQTST calculation, and they are therefore not allowed to carry flux across the surface. As $^3\Sigma$ states are added to the electrotational basis, the energy correlation diagram for these states is likely to be lowered and a much greater total reactivity from the $^2P_{\frac{1}{2}}$ initial state of fluorine may be observed.

IV. Summary and Conclusions

Electronic-rotational energy transfer has been studied in low energy $F(^2P) + H_2$ three-dimensional collisions through use of the R-matrix propagation method to integrate the quantum mechanical close-coupling equations. The electrotational basis functions used to expand the scattering wavefunction are sums of products of DIM electronic functions and nuclear rotational functions. Transition probabilities, yields, and cross sections were presented for the inelastic quenching of electronically excited F atoms, with and without the presence of simulated reaction channels (introduced via DQTST). In the quenching process $F(^2P_{\frac{1}{2}}) + H_2(j=0) \rightarrow F(^2P_{3/2}) + H_2(j')$, near-resonant

(j'=2) collisions highly dominate over non-resonant (j'=0) ones. The interesting interweaving of resonant transition probabilities for even and odd nuclear parity as the total angular momentum increases was related to the distance and energy dependence of avoided crossing structure in adiabatic electrotational energy correlation diagrams. The tendency for quenching to occur in fairly localized regions at large atom-molecule separations was confirmed by neglecting inter-channel overlap in the R-matrix propagation scheme. The resultant quenching probabilities were only about 1/5 of the "exact" values. In addition, it was found that open reaction channels had little effect on the low energy quenching probabilities. Further study needs to be made of the sensitivity of the results to the form of the long-range F-H_2 potential. In addition, the influence of open reaction channels needs to be more accurately studied, particularly at higher energies.

Acknowledgement

These calculations were initiated at the "Workshop on Reactive Collisions" sponsored by CECAM at the University of Paris (Orsay). We thank Carl Moser for his encouragement and hospitality.

References

1. J. C. Tully in W. H. Miller (ed.), "Modern Theoretical Chemistry: Molecular Collisions, Part B" (Plenum, 1970).
2. J. C. Tully in P. R. Brooks and E. F. Hayes, "State-to-State Chemistry," ACS Symp. Series 56, 206 (1977).
3. I. H. Zimmerman and T. F. George, J. Chem. Phys. 61, 2468 (1974); 63, 2109 (1975); Chem. Phys. 7, 323 (1975).
4. J. M. Bowman, S. Leasure, and A. Kuppermann, Chem. Phys Lett. 43, 374 (1976).
5. Z. H. Top and M. Zaer, Chem. Phys. 25, 1 (1977).
6. S. Chu and A. Dalgarno, J. Chem. Phys. 62, 4009 (1975).
7. F. H. Mies, Phys. Rev. A7, 942, 957 (1973).
8. P. L. DeVries and T. F. George, Chem. Phys. Lett. 43, 391 (1976); J. Chem. Phys. 66, 2421 (1977).
9. F. Rebentrost and W. A. Lester, Jr., J. Chem. Phys. 63, 3737 (1975), ibid., 64, 3879 (1976).
10. F. Rebentrost and W. A. Lester, Jr., J. Chem. Phys. 67, 3367 (1977).
11. J. C. Tully, J. Chem. Phys. 60, 3042 (1974).
12. A. Komornicki, K. Morokuma, and T. F. George, J. Chem. Phys. 67, 5012 (1977); ibid. 65, 4312 (1976).
13. J. C. Tully, J. Chem. Phys. 58, 1396 (1973).
14. J. C. Tully, J. Chem. Phys. 59, 5122 (1973).
15. D. L. Miller and R. E. Wyatt, Chem. Phys. Lett. 38, 410 (1976).
16. P. L. DeVries and T. F. George, J. Chem. Phys. 67, 1293 (1977).

17. D. L. Miller and R. E. Wyatt, J. Chem. Phys. 67, 1302 (1977).

18. R. A. Marcus, J. Chem. Phys. 49, 2610 (1968).

19. R. E. Wyatt, J. Chem. Phys. 56, 390 (1972).

20. a) J. C. Light and R. B. Walker, J. Chem. Phys. 65, 4272 (1976).

b) D. Zvijac and J. C. Light, Chem. Phys. 12, 237 (1976).

c) J. C. Light, Methods Comp. Phys. 10, 111 (1977).

21. J. C. Light and A. Altenberger-Siczek, Chem. Phys. Lett. 30, 195 (1975).

22. R. B. Walker, to be published.

23. S. H. Harms, A. B. Elkowitz and R. E. Wyatt, Mol. Phys. 31, 177 (1976).

24. E. Merzbacher, "Quantum Mechanics" (Wiley, New York, 1961).

Figure Captions

Fig. 1. Collision coordinates in collinear subspace. Z and z are the components of $\vec{R}$ and $\vec{r}$ on the rotating z-axis. Point P is located by coordinates (s,ρ), where s is the arc length measured along the reference curve (RC), with s = 0 on the reactant-product match surface (M). In the polar region ($s > s_p$), the RC is a circular arc centered at the turning center (TC). The minimum energy reaction path is RP. R_p, r_p, and Ψ are geometric quantities which appear in the rotational moments of inertia. For noncollinear geometries, coordinates ρ and γ are used within each constant s-plane.

Fig. 2. Near-resonant transition probabilities for $F(^2P_{\frac{1}{2}}) + H_2(0) \rightarrow F(^2P_{3/2}) + H_2(2)$ vs. J at (a) 0.012 eV and (b) 0.035 eV. Both even (——) and odd (---) nuclear parities are shown.

Fig. 3. Near-resonant and nonresonant quenching probabilities vs. E_{tr} (translational energy measured from the $F(^2P_{\frac{1}{2}}) + H_2(j=0)$ energy). Eight electrotational channels were included in the scattering basis at $J = \frac{1}{2}$.

Fig. 4. Inelastic cross sections (a_o^2) and yield for near-resonant and nonresonant $F(^2P_{\frac{1}{2}}) + H_2(j=0)$ collisions, as a function of translational energy (eV).

Fig. 5. $F + H_2$ electrotational energy correlation diagram. The eigenvalues of the local coupling matrix are plotted as a function of the reaction coordinate s for total angular momentum $J = 0.5$. In a, all states asymptotically correlating to $J_F = 0.5$, $j = 0, 2, 4$ and $J_F = 1.5$, $j = 0, 2$ are included in the basis. Note the repulsive nature of the interaction as $|s| \to 0$. In b, the scale is expanded to show the avoided crossing between the $J_F = 0.5$, $j = 0$ state and two of the states originating from the $J_F = 1.5$, $j = 2$ manifold. The crossing occurs here between $s = -4.8$ and -5.8 bohrs.

Fig. 6. $F + H_2$ electrotational energy correlation diagrams. The detailed structure of the avoided crossing region between the $J_F = 0.5$, $j = 0$ state and the $J_F = 1.5$, $j = 2$ states is shown. The splitting of the lower manifold is due to the various possibilities for ℓ and L_n. In a - f respectively, we show the correlation diagram for the positive nuclear parity $J = 6.5$, 7.5, 8.5, and negative nuclear parity $J = 6.5$, 7.5, 8.5 cases. Note that the crossing points move to higher energies and larger values of $|s|$ as the total angular momentum is increased. The alternating character of the crossing points (in and out in s and up and down in energy) correlates directly with the interwoven structure of the resonant transition probabilities of Fig. 2.

Fig. 7. Effect of neglect of interstate mixing in the interval (s_{min}, s_{max}) on the near-resonant quenching probability, for $J = \frac{1}{2}$ (even nuclear parity). The "exact" probability curve is also shown for comparison.

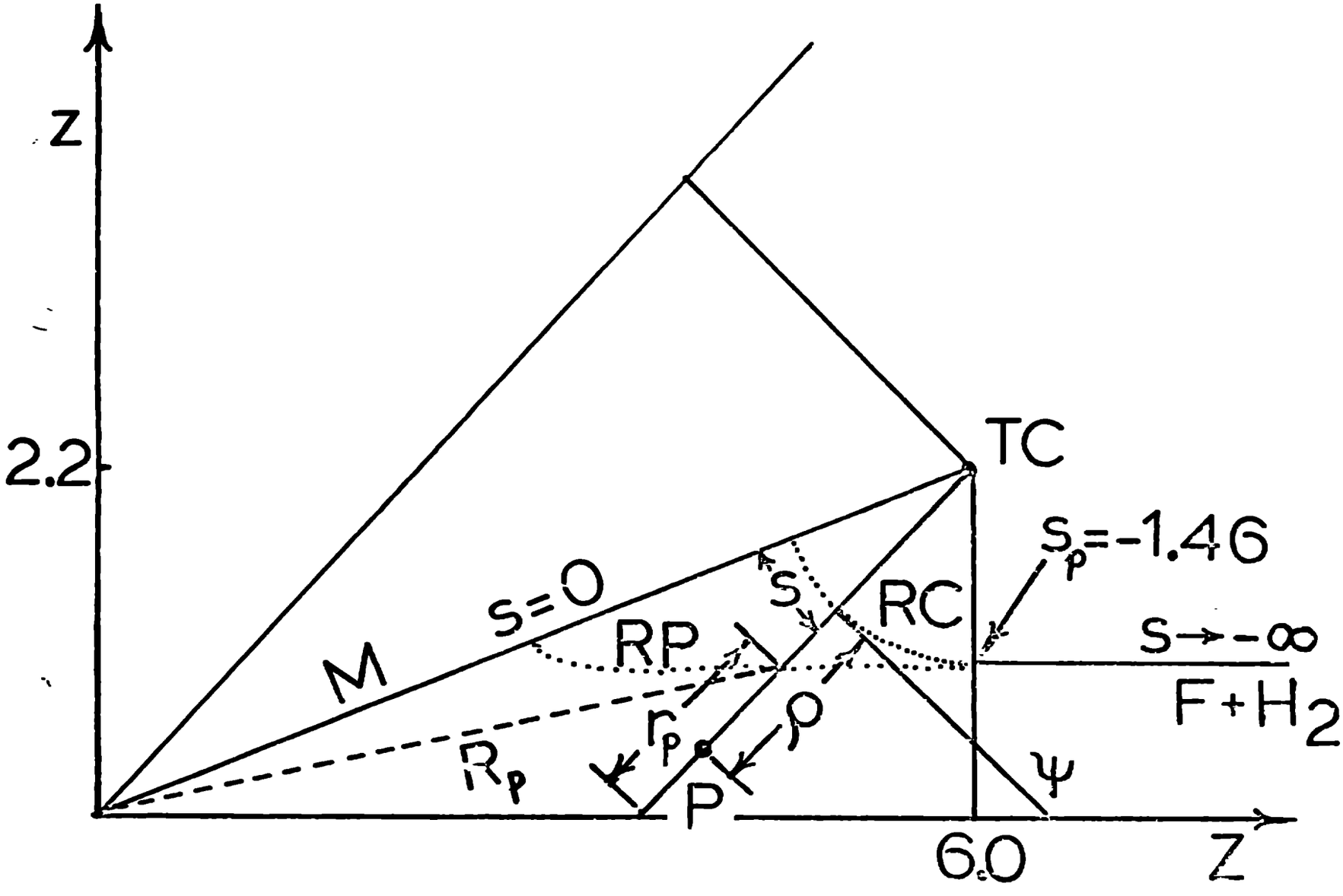
z
2.2
TC
$s_p = -1.46$
s=0
s
RC
RP
$s \to -\infty$
M
$F + H_2$
r_p
ρ
R_p
ψ
P
6.0
Z

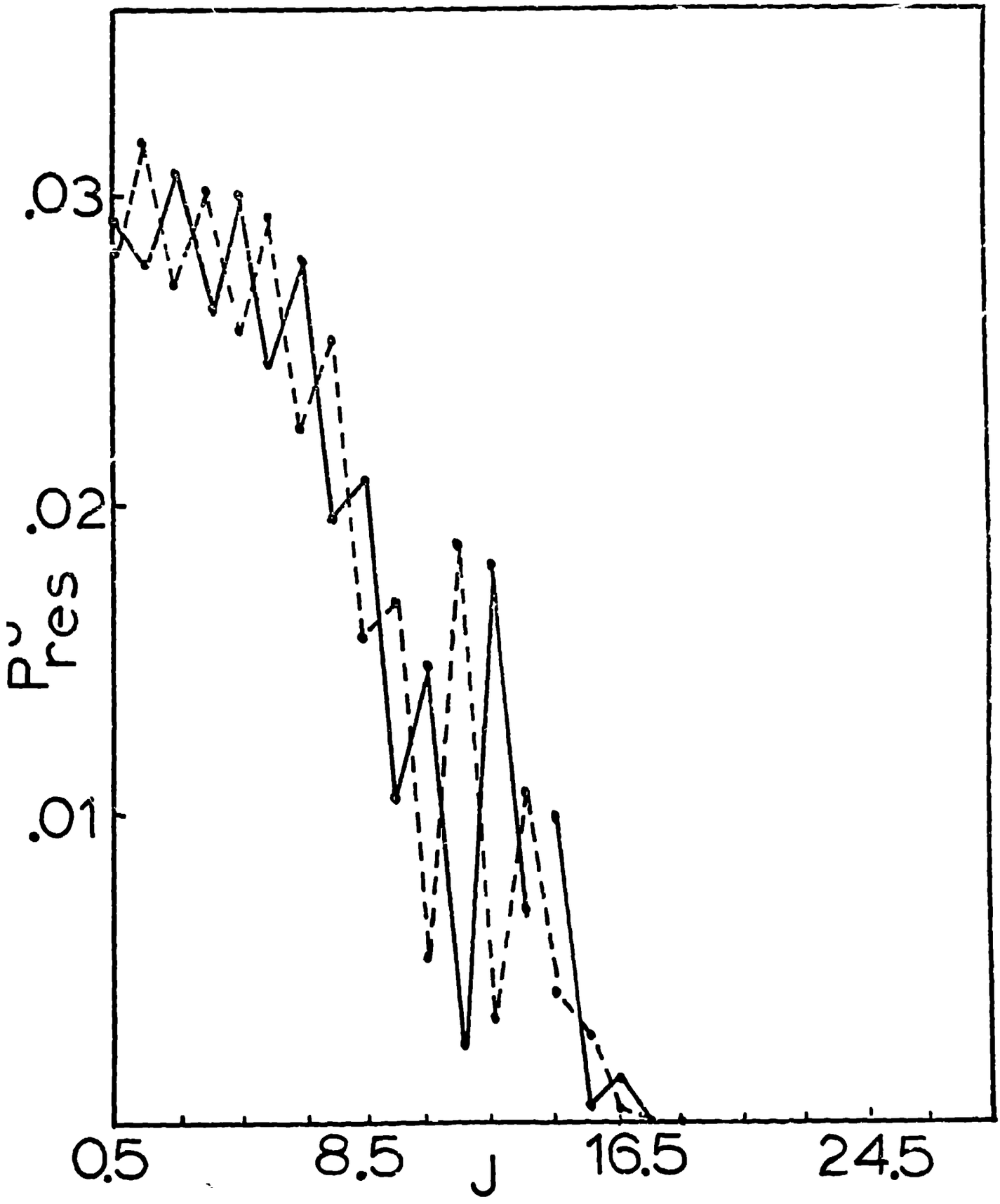
.03
.02
.01
P'_{res}
0.5
8.5
16.5
24.5
J

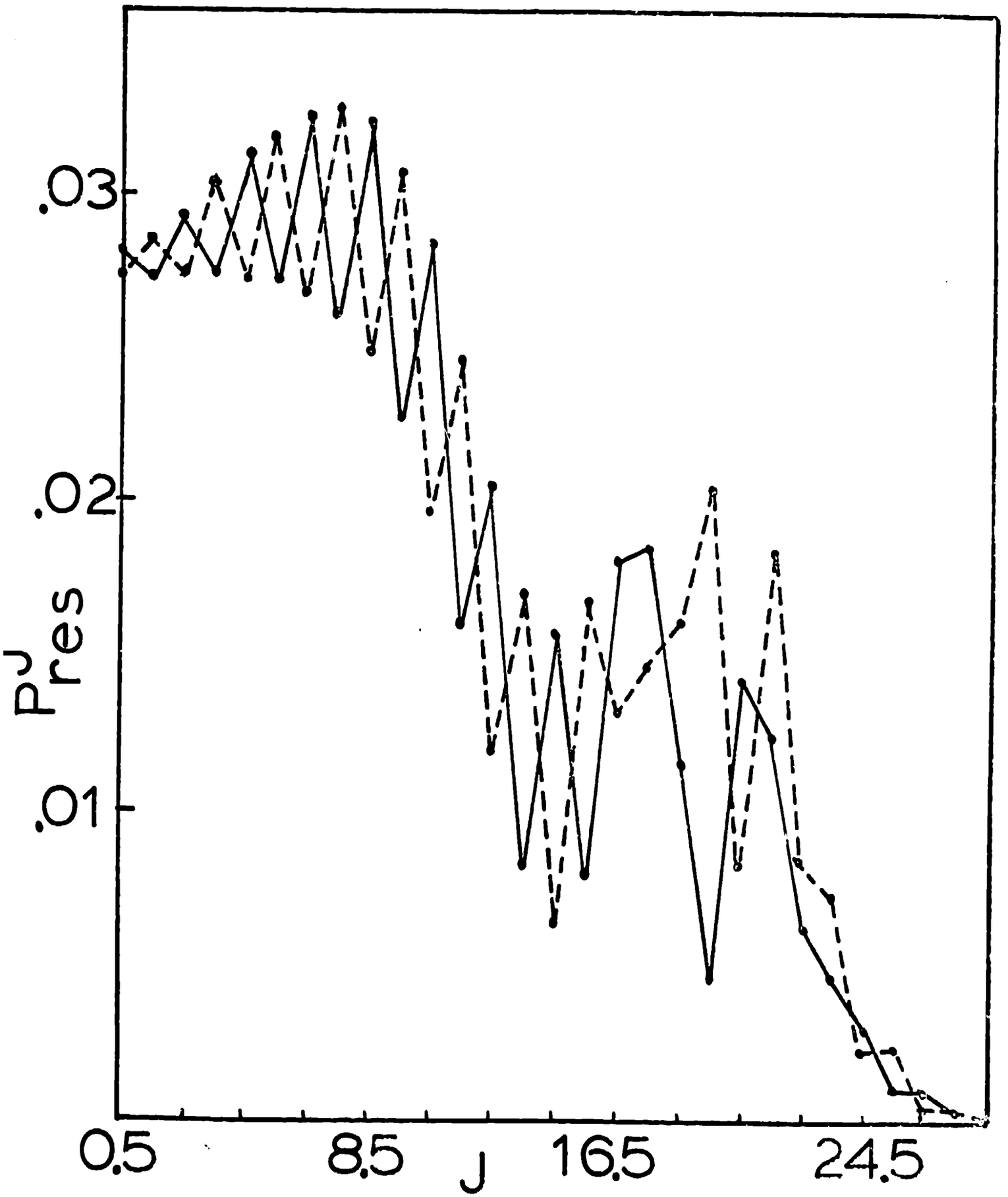
.03
.02
.01
P^J_{res}
0.5
8.5
J
16.5
24.5

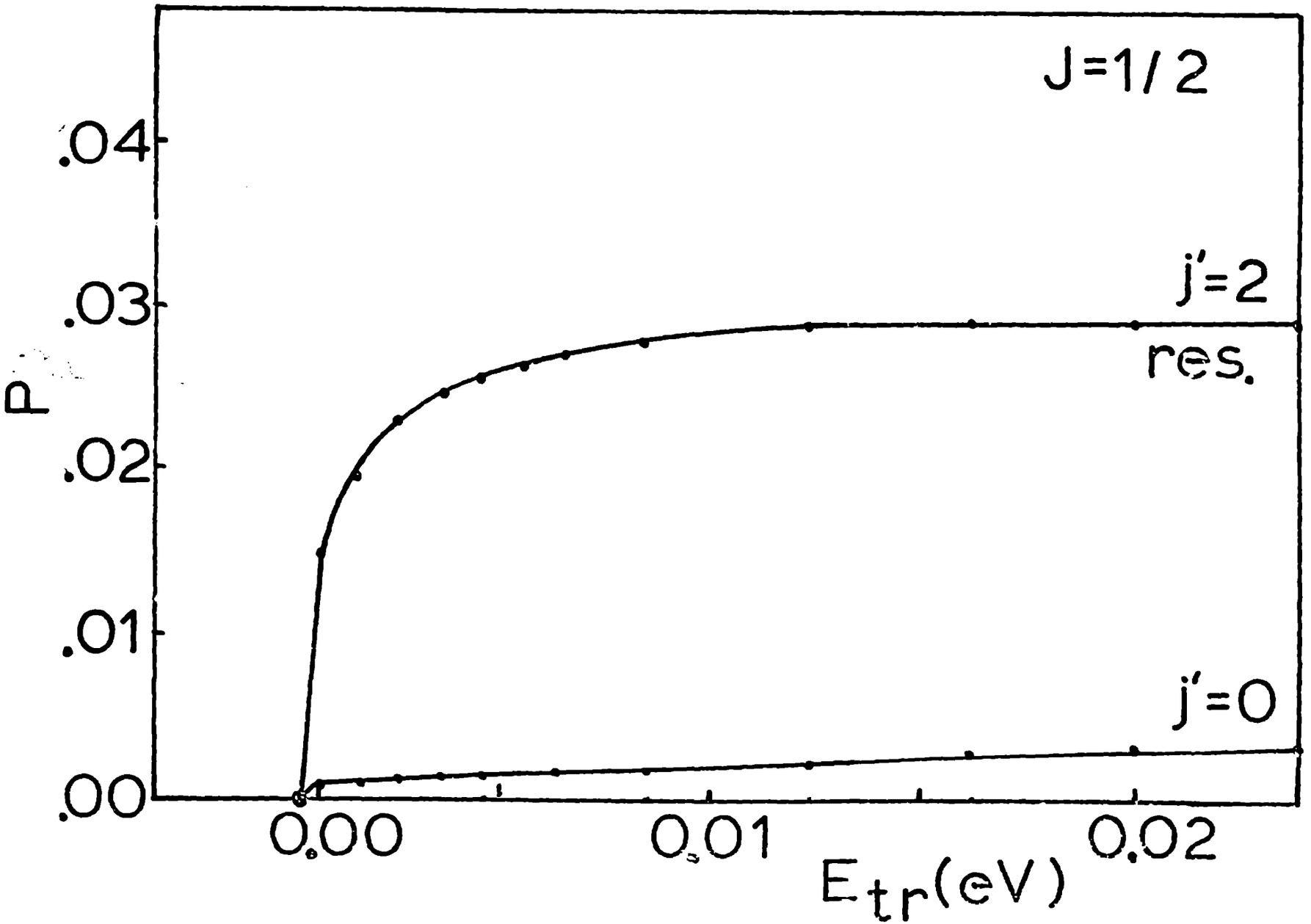
J=1/2
j'=2
res.
j'=0
.04
.03
.02
.01
.00
P
0.00
0.01
0.02
E_{tr}(eV)

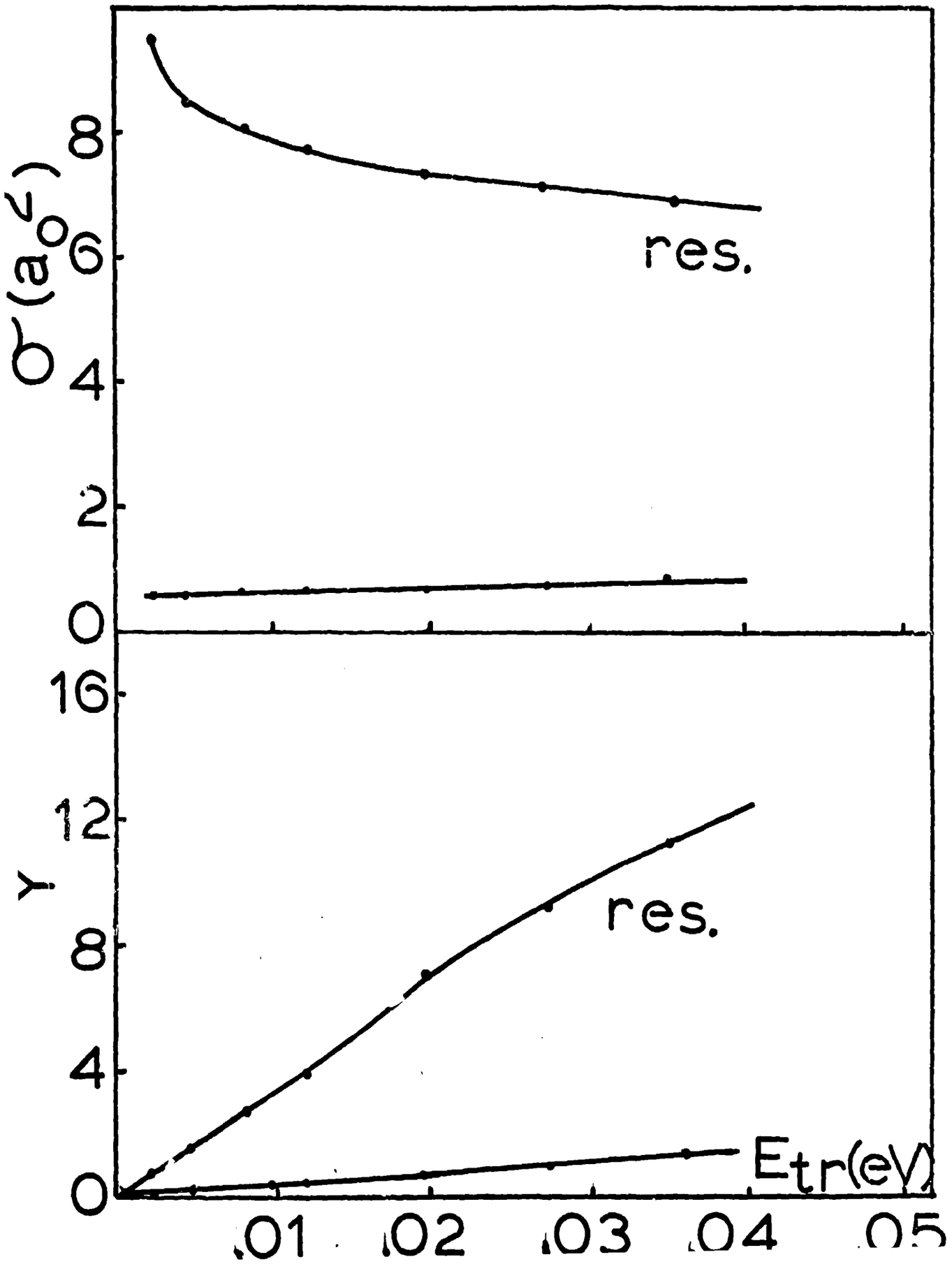
σ (a₀²)
8
6
4
2
0
res.
16
12
8
4
0
Y
res.
Etr(eV)
.01
.02
.03
.04
.05

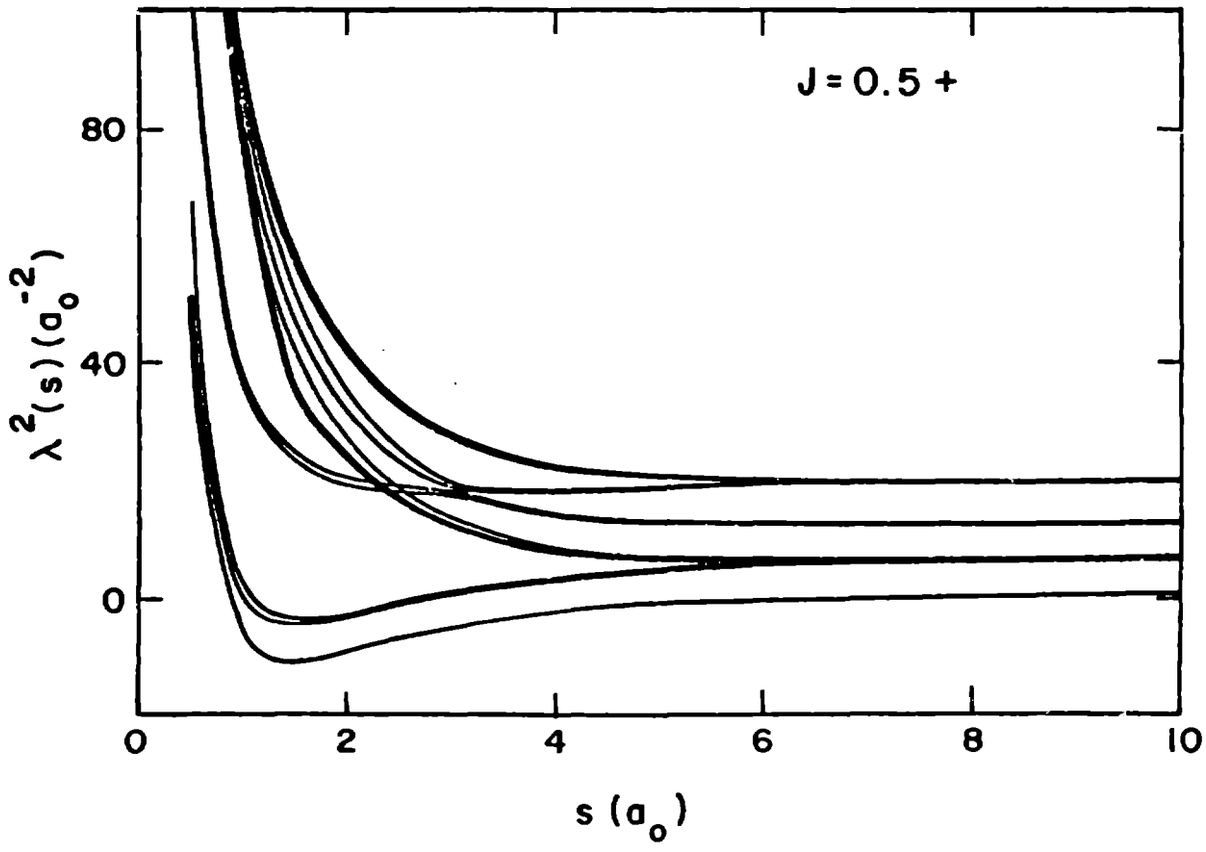

5a

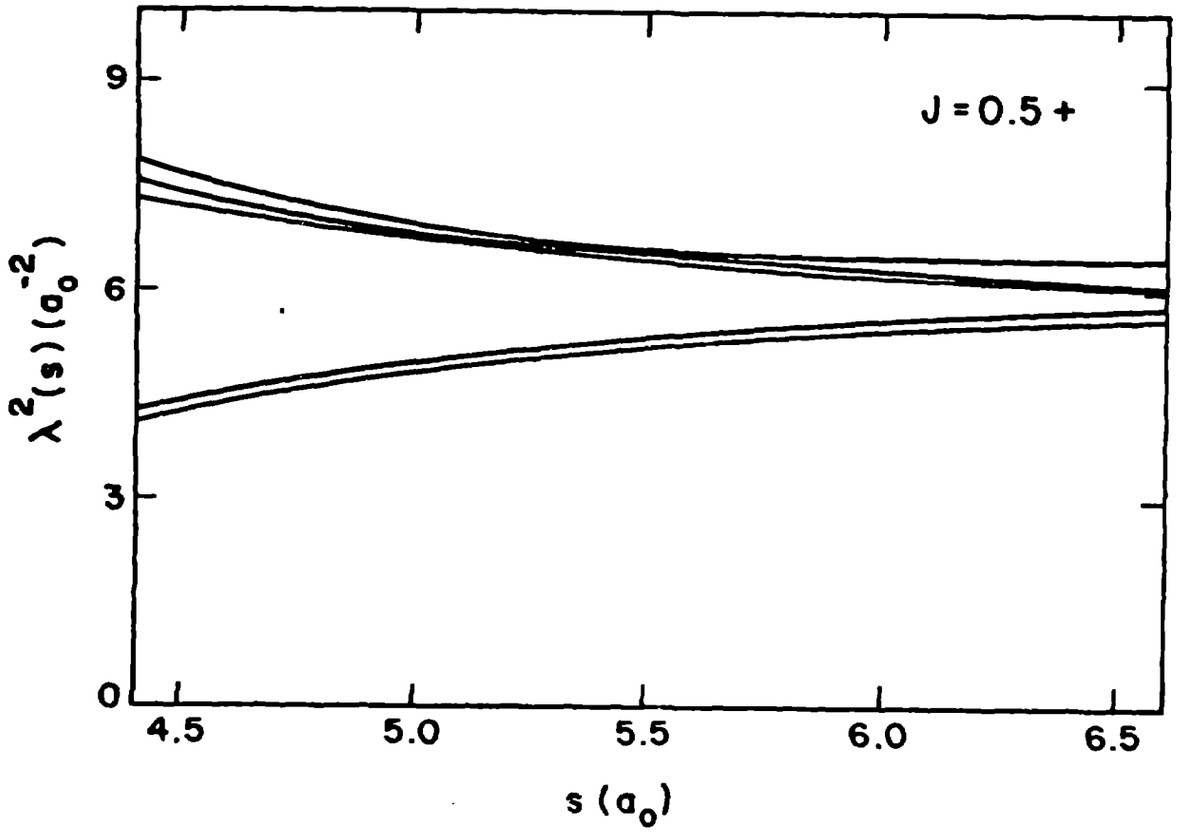
J = 0.5 +
9
6
3
0
4.5
5.0
5.5
6.0
6.5
$\lambda^2(s)\,(a_0^{-2})$
$s\,(a_0)$

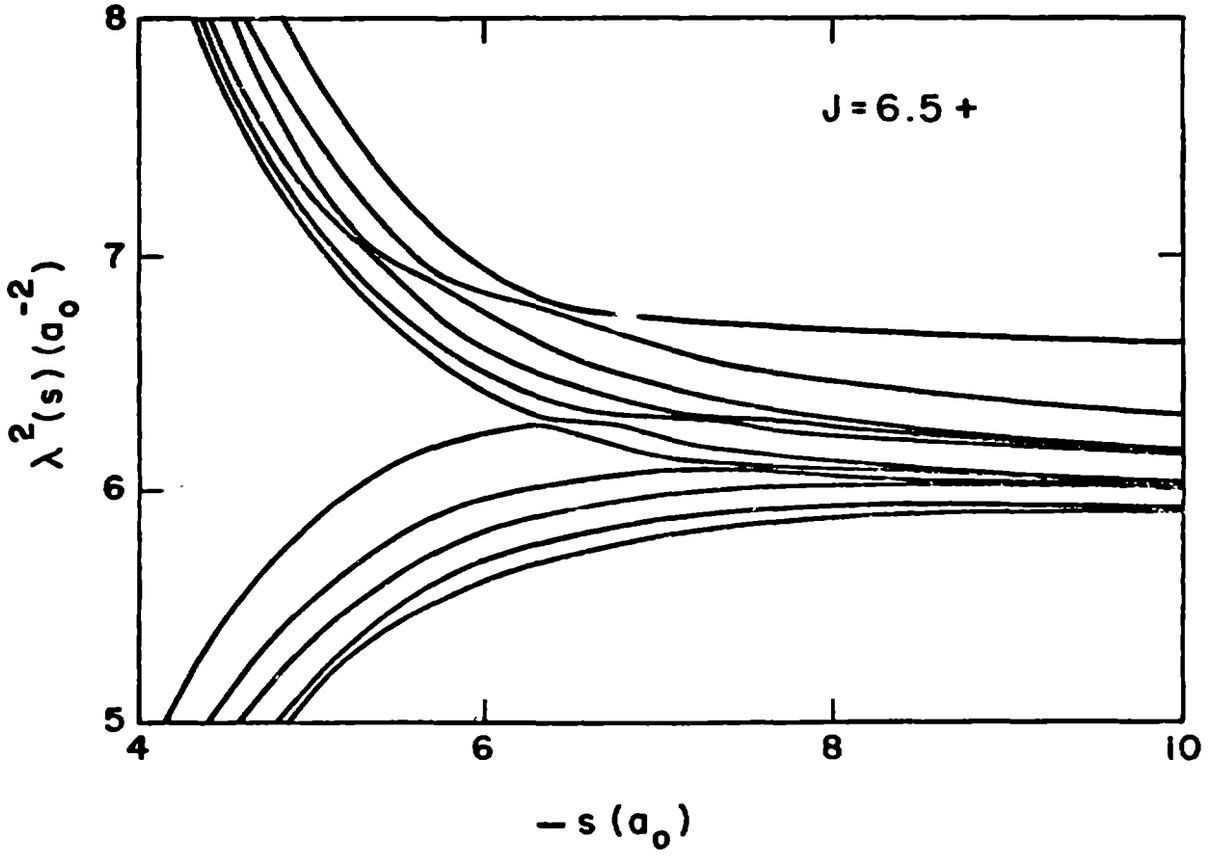
J = 6.5 +
$\lambda^2(s)\,(a_0^{-2})$
$-s\,(a_0)$
8
7
6
5
4
6
8
10

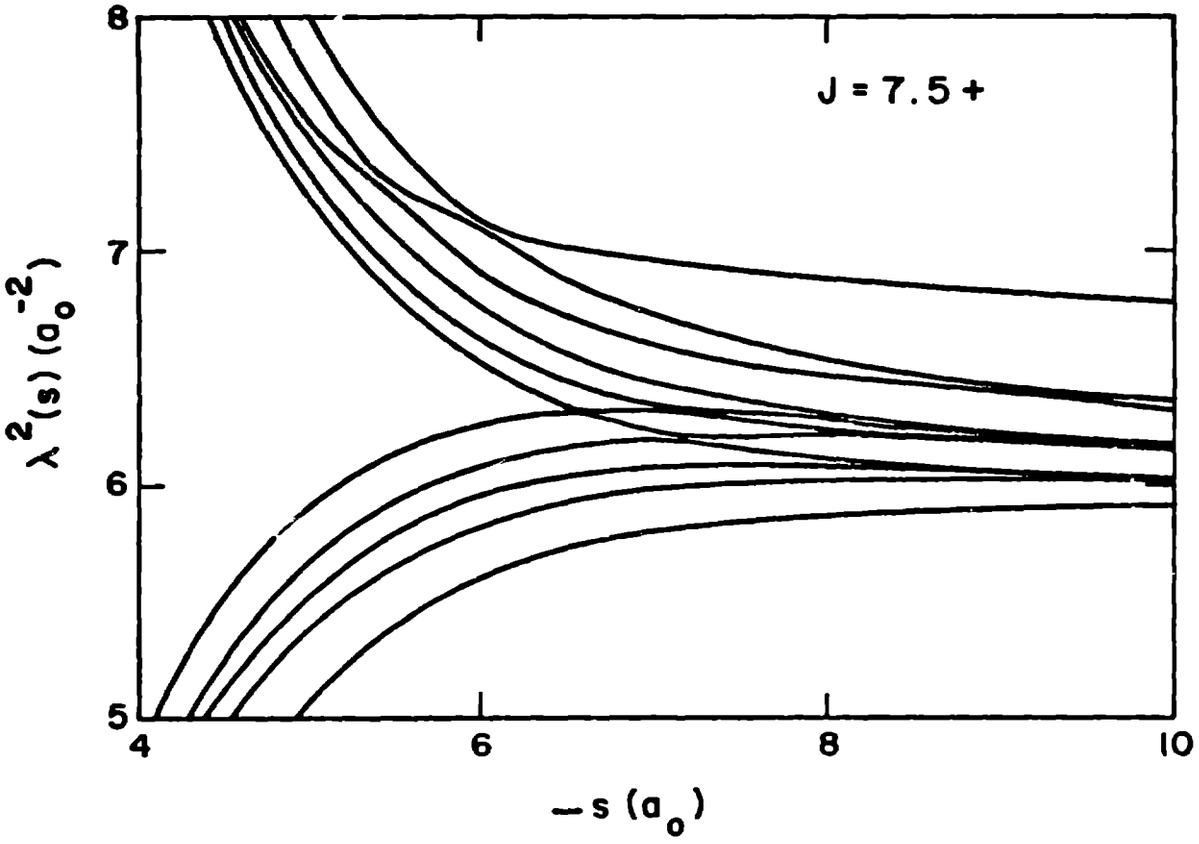
J = 7.5 +
8
7
6
5
4
6
8
10
$\lambda^2(s)\ (a_o^{-2})$
$-s\ (a_o)$

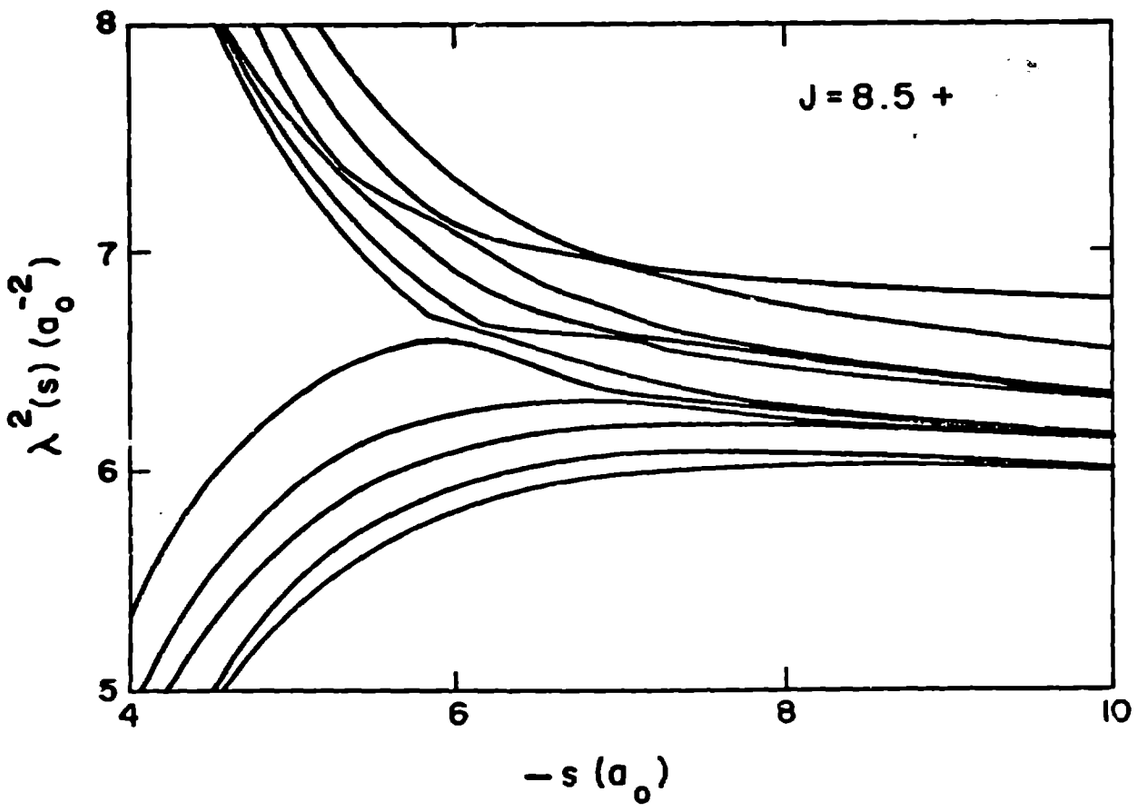
J = 8.5 +
$\lambda^2(s)\ (a_0^{-2})$
$-s\ (a_0)$
8
7
6
5
4
6
8
10

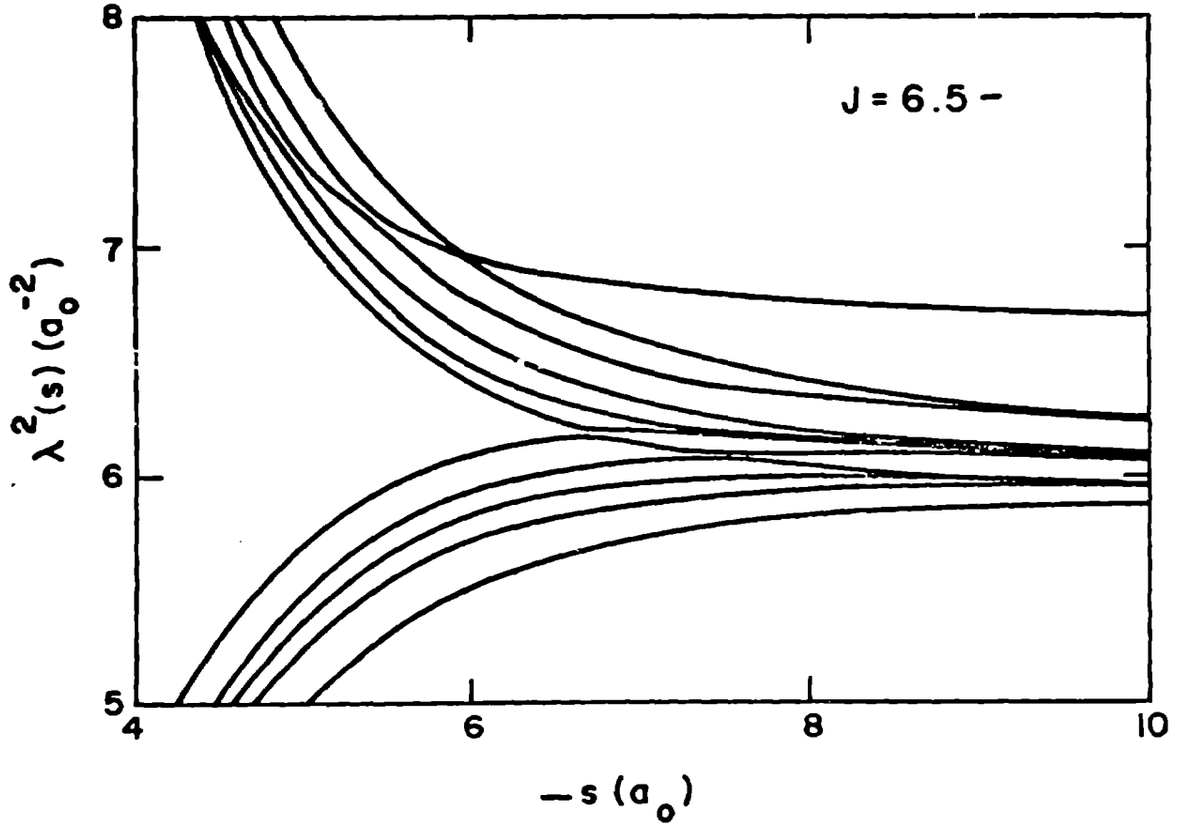
J = 6.5 −
8
7
6
5
4
6
8
10
$\lambda^2(s)\ (a_0^{-2})$
$-s\ (a_0)$

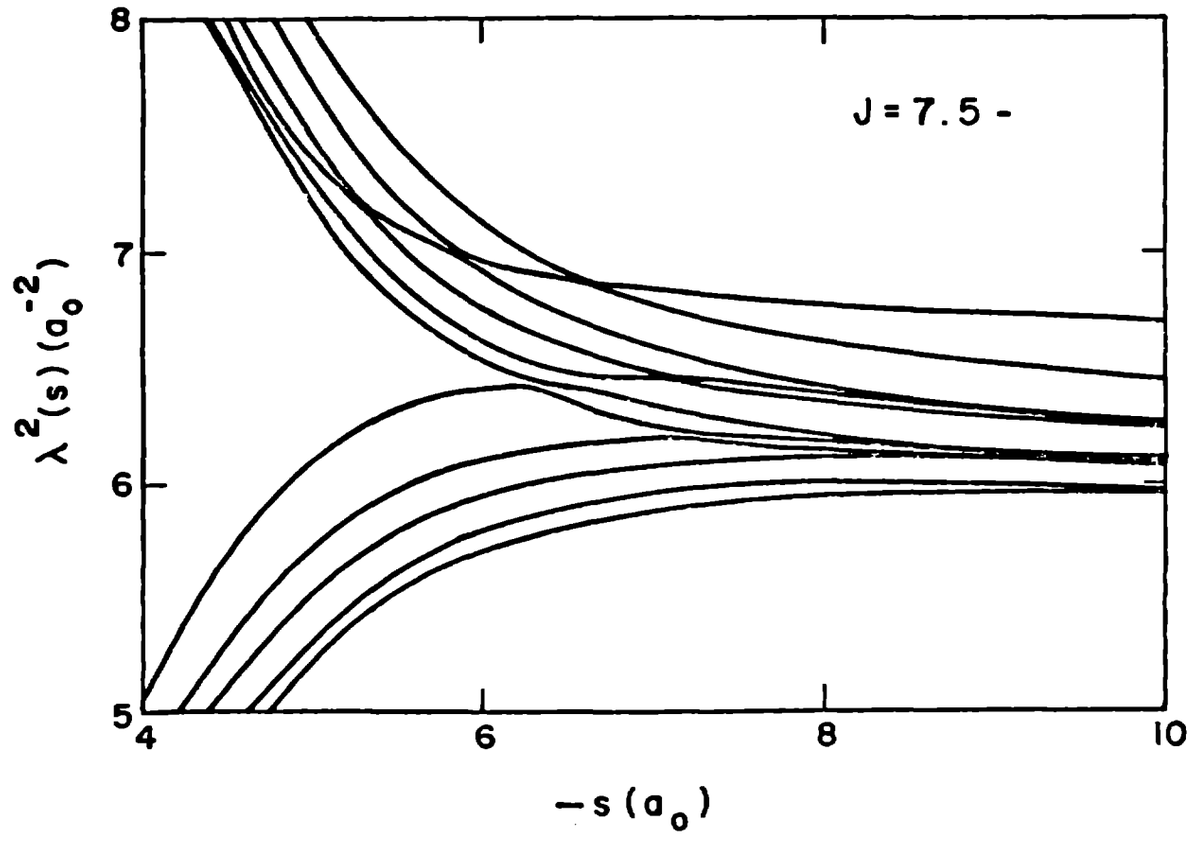
J = 7.5 -
8
7
6
5
4
6
8
10
$\lambda^2(s)\,(a_0^{-2})$
$-s\,(a_0)$

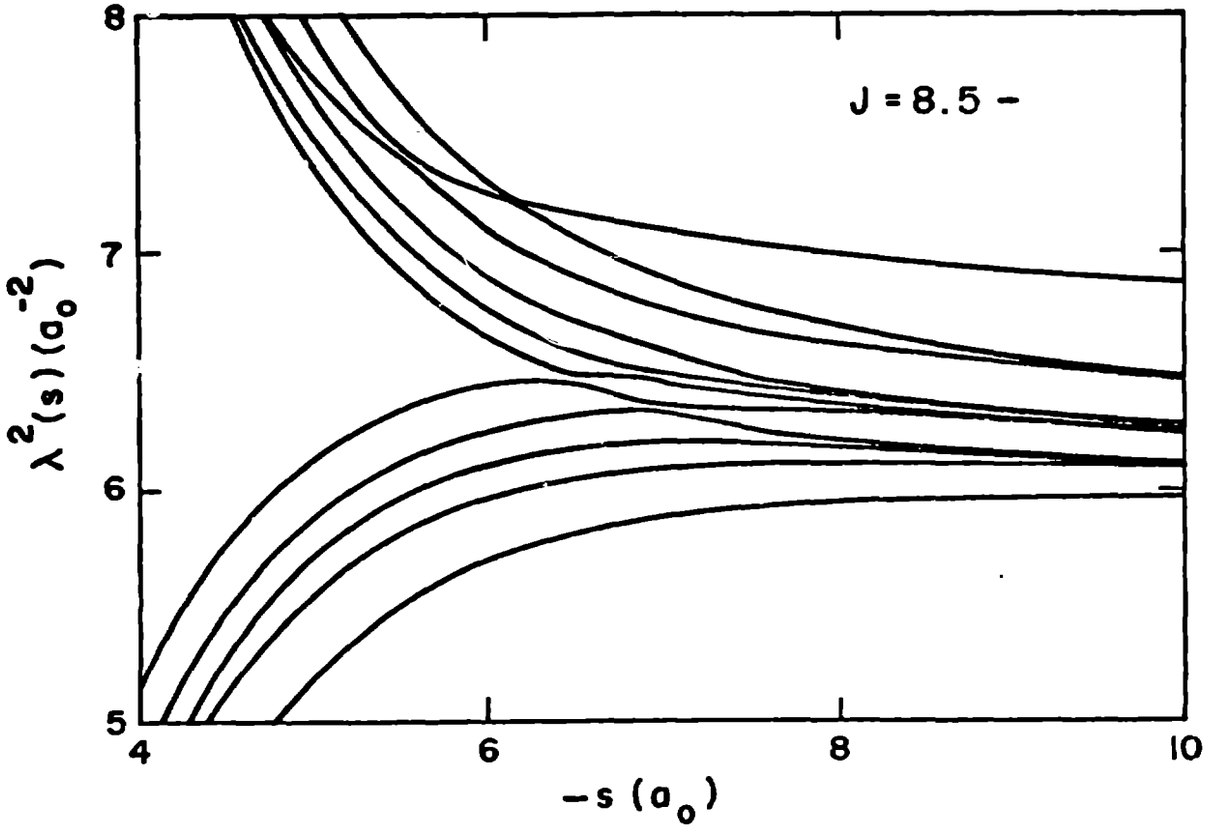
J = 8.5 −
$\lambda^2(s)\,(a_0^{-2})$
8
7
6
5
4
6
8
10
$-s\,(a_0)$

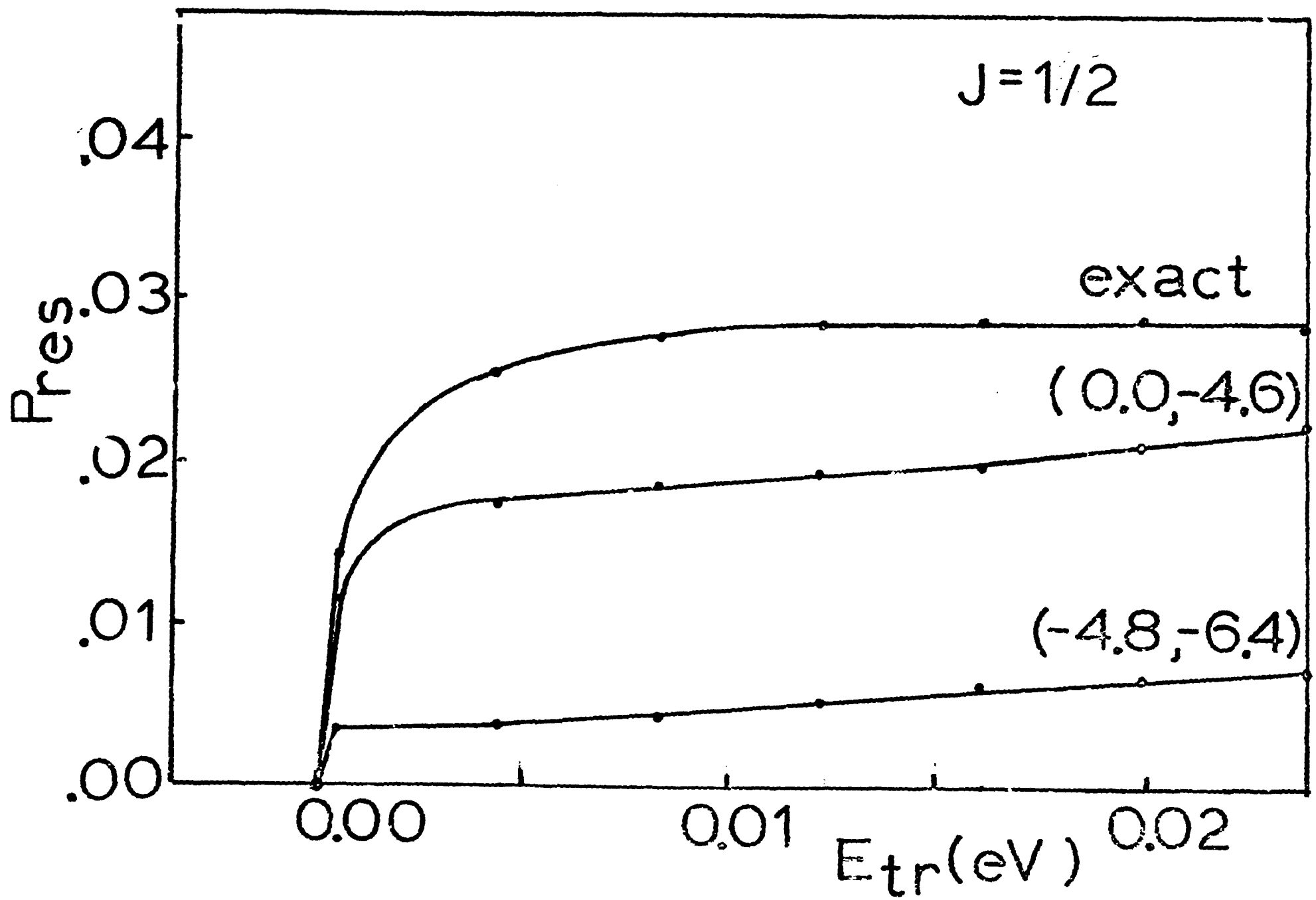
J=1/2
exact
(0.0,-4.6)
(-4.8,-6.4)
.04
.03
.02
.01
.00
Pres.
0.00
0.01
0.02
Etr(eV)